Automatic dendritic spine segmentation in widefield fluorescence images reveal synaptic nanostructures distribution with super-resolution imaging

Jiahao Zhang[1], Rohit Vaidya[2], Hee Jung Chung[3], Paul R. Selvin[1,2,†]

[1]Dept. of Physics, University of Illinois at Urbana-Champaign, Urbana, IL, USA

[2]Center for Biophysics and Quantitative Biology, University of Illinois at Urbana-Champaign, Urbana, IL, USA

[3]Department of Molecular and Integrative Physiology, University of Illinois at Urbana-Champaign, Urbana, IL, USA

[†]Corresponding author

SUMMARY

Dendritic spines are the main sites for synaptic communication in neurons, and alterations in their density, size, and shapes occur in many brain disorders. Current spine segmentation methods perform poorly in conditions with low signal-to-noise and resolution, particularly in the widefield images of thick (≥ 10 μm) brain slices. Here, we combined two open-source machine-learning models to achieve automatic 3D spine segmentation in widefield diffraction-limited fluorescence images of neurons in thick brain slices. We validated the performance by comparison with manually segmented super-resolution images of spines reconstructed from direct stochastic optical reconstruction microscopy (dSTORM). Lastly, we show an application of our approach by combining spine segmentation from diffraction-limited images with dSTORM of synaptic protein PSD-95 in the same field-of-view. This allowed us to automatically analyze and quantify the nanoscale distribution of PSD-95 inside the spine. Importantly, we found the numbers, but not the average sizes, of synaptic nanomodules and nanodomains increase with spine size.

INTRODUCTION

Dendritic spines are small postsynaptic protrusions from neuronal dendrites that contain most of the excitatory synapses in the brain and provide the morphological basis for synaptic plasticity.[1,2] Spines are highly dynamic. New spines are formed while others are eliminated in response to development and experience, and their size and shape can change over the scale of seconds to minutes.[1,3–7] Moreover, alterations in the spine density, size, and shape are common hallmarks in many neurodegenerative,[8] neurodevelopmental,[9] and neuropsychiatric[10] disorders.

It is therefore important to quantify changes in the density and morphologies of dendritic spines, as well as molecular changes occurring within them, across wide brain regions and with high temporal resolution. Hence, there exists a need for accurate spine segmentation methods—i.e., delineating and separating different spines—for fast imaging modalities, particularly in intact brain tissue. Fast and easily accessible imaging modalities, however, generally lead to images with lower signal-to-noise (SNR) and resolution. Fluorescence imaging under a widefield microscope, where neurons and their spines are labeled with a dye or a fluorescent protein, a readily accessible method with relatively fast imaging speed. However, existing spine segmentation methods for fluorescence microscopy are primarily designed for confocal 1- or 2-photonmicroscopy, which generally have higher SNR and resolution.[11–19] In addition, for widefield imaging, manually segmenting the spines instead of applying an automatic method, can potentially introduce human biases and require significantly more time which counteracts the benefit of imaging speed.

To overcome this challenge, we established a novel approach by combining two existing open-source machine-learning models, DeepD3[20] and Stardist.[21] DeepD3, a model developed for spine detection, is first used to determine the likelihood that a sub-diffraction-limited pixel is part of a spine. Stardist, a model originally developed for nuclei segmentation, is then used to segment the spines based on the fluorescence intensity within the pixels predicted by DeepD3. Separating the segmentation step via Stardist from the detection step via DeepD3, as well as utilizing the fluorescence intensity in both DeepD3 and Stardist, gives a more accurate determination of spine regions than using DeepD3 alone. Most importantly, overlapping spines and the spine-neck regions within spines are well separated, whereas traditional segmentation methods such as Watershed[22] fail. Combined with slightly further processing, this approach enables automatic 3D spine segmentation in widefield diffraction-limited fluorescence images of neurons in thick brain slices.

To validate our approach using DeepD3+Stardist, we performed super-resolution dSTORM[23,24] imaging of the neuron. dSTORM falls under the category of single-molecule localization microscopy (SMLM), which utilizes individual fluorescent molecules blinking and subsequent localizations to provide significantly improved spatial resolution over traditional diffraction-limited or confocal microscopy.[25] We compared the segmentation of diffraction-limited images by DeepD3+Stardist with the manually segmented dSTORM images (See SI). Manual segmentation is generally used as the benchmark—or the “ground truth”. We would expect yet more accurate validation data when using the high-resolution dSTORM, instead of the human annotatition of the original images traditionally used.

Beyond its utility in validation of segmentation, we have used dSTORM to image and characterize the nanoscale distribution of molecular targets, i.e. the distribution of

proteins within a spine. With the segmentation derived from DeepD3+Stardist, we show the capability for spine-specific analysis of synaptic proteins imaged by dSTORM in 30 μm brain slices.[26] We performed nanobody labeling and dSTORM imaging on the post-synaptic protein PSD-95, which is critically involved in anchoring AMPA and NMDA receptors to the excitatory synapse.[27,28] We find that the number of synaptic nanomodules, which are sub-diffraction modules of synaptic proteins inside a spine and linked to its structural plasticity, increases with spine size, as previously was seen by STED.[29] By calculating the size/volume of nanomodules, we also found that the average size of nanomodules inside a spine does *not* depend on the spine size.

Furthermore, as a benefit of SMLM, we examined the distribution of postsynaptic nano*domains*, which are highly concentrated regions inside of nanomodules within spines. They are ~ 70 or 80 nm in size and not resolvable with the resolution of STED.[30,31] The organization of postsynaptic nanodomains are aligned to the presynaptic release sites of trans-synaptic nanocolumns, which regulates synaptic transmission and plasticity.[30–34] We found that the number of nanodomains inside a nanomodule increases with the nanomodule size. Lastly, the ratio of the number of nanodomains to nanomodules does *not* change with spine size; this signifies that the total number of nanodomains, i.e., the number of nanomodules times the ratio, also increases with spine size.

RESULTS

Automatic 3D dendritic spine segmentation for low signal-to-noise and resolution fluorescence images

Here, we describe our automatic 3D dendritic spine segmentation approach. It is applicable to the low SNR and resolution conditions in widefield fluorescence imaging in thick brain slices. We combine two existing open-source machine-learning models, DeepD3 and Stardist. DeepD3 is an open framework developed for automated quantification of the number of dendritic spines. It is trained on human annotated data and has been demonstrated to work for one-photon confocal and *ex vivo* and *in vivo* two-photon images taken for different fluorescent labels, species, and brain regions. However, while it determines the number of spines, its 3D segmentation function does not accurately capture the 3D spine shapes, which is useful for determining the volumes and/or types of spines. The 3D segmentation failed for our widefield fluorescence data, even when a small step size (of 25 nm) in the z-direction was used to capture the 3D spine shapes. In addition, the program uses the traditional Watershed segmentation method, which cannot accurately separate overlapping spines and spine neck from the head region, important for determining both the number and shapes of the spines. Therefore, we combine DeepD3 with Stardist, an open-source model originally

developed for nuclei segmentation, to accurately segment the spines utilizing the fluorescent intensity within regions.

The diagram of the workflow for creating 3D segmentation of spines is shown in Figure 1A. After obtaining the fluorescent z-stack of the neuron (Fig. 1A-1), background subtraction is applied to reduce background noise in the image (Fig. 1A-2). Then, for each frame of the z-stack, DeepD3 is used to assign a prediction value of each pixel for its likelihood to be part of a spine (Fig. 1A-3). A binary mask is then created by using a prediction value threshold, which is set relatively low, so pixels neighboring the spine regions are included (Fig. 1A-4). This binary mask is mapped back to the original fluorescence image (Fig. 1A-5), and the fluorescence intensity information within the masked regions is extracted (Fig. 1A-6). The intensities inside these regions are used by Stardist to perform 2D segmentation of the spines in each frame (Fig. 1A-7). Finally, the 2D segmentations across different z-axis frames are connected based on overlap to create the 3D segmentation (Fig. 1A-8).

Using DeepD3+Stardist, we can reliably separate overlapping spines, as well as the head and neck regions within a singular spine. Figure 1B-1a (the region of interest, ROI, 1 of Figure 1A-8) shows that two partially overlapping but visually separable spines are initially and correctly separated by both DeepD3+Watershed (Figure 1B-1b) and DeepD3+Stardist (Figure 1B-1c). However, for the image in the next frame located just 25 nm above (Figure 1B-1’a), DeepD3+Watershed fails to separate the two spines again (Figure 1B-1’b) whereas DeepD3+Stardist gives a consistent segmentation (Figure 1B-1’c). For the DeepD3+Watershed segmentation, this results in the two 3D regions being connected and hence incorrectly considered to be from the same spine.

In terms of separating the head and the neck regions of the spine (Figure 1B-2a; ROI 2 of Figure 1A-8), DeepD3+Watershed fails (Figure 1B-2b). In contrast, they are distinguished by DeepD3+Stardist (Figure 1B-2c). Furthermore, we need to correctly assign which of the two regions is the head and which is the neck. To do this, a single line that represents the neck is created to connect each segmented region to the dendrite detected by DeepD3, as shown in Figure 1C. A segmented region which is crossed by a “neck line” of another region is assigned as a neck region of the spine. This can be used to determine the neck lengths because the necks of many spines are invisible in the widefield images due to the low SNR and resolution.

An additional trimming process may also be added to remove low-intensity pixels that may be incorrectly assigned to be part of the spine in the 3D segmented results. For each segmented spine, a cutoff intensity is calculated as a user-defined ratio (which can be adjusted according to the imaging quality) times its average fluorescence intensity. Pixels with intensity below the cutoff intensity are removed from the segmented spine regions. Figure 1D-3a and 1D-4a (ROI 3 and 4 of Figure 1A-8) shows two example

spines, and the segmented results after an additional intensity trimming step (Figure 1D-3c and 1D-4c). The resulting image matches the original fluorescent image more closely than before trimming (Figure 1D-3b and 1D-4b). Even though this step appeared to improve the match with actual spine shapes in some cases, for our overall validation data, we did not find it necessary given the parameters we used in segmentation. However, this might be beneficial for a different imaging condition or set of segmentation parameters.

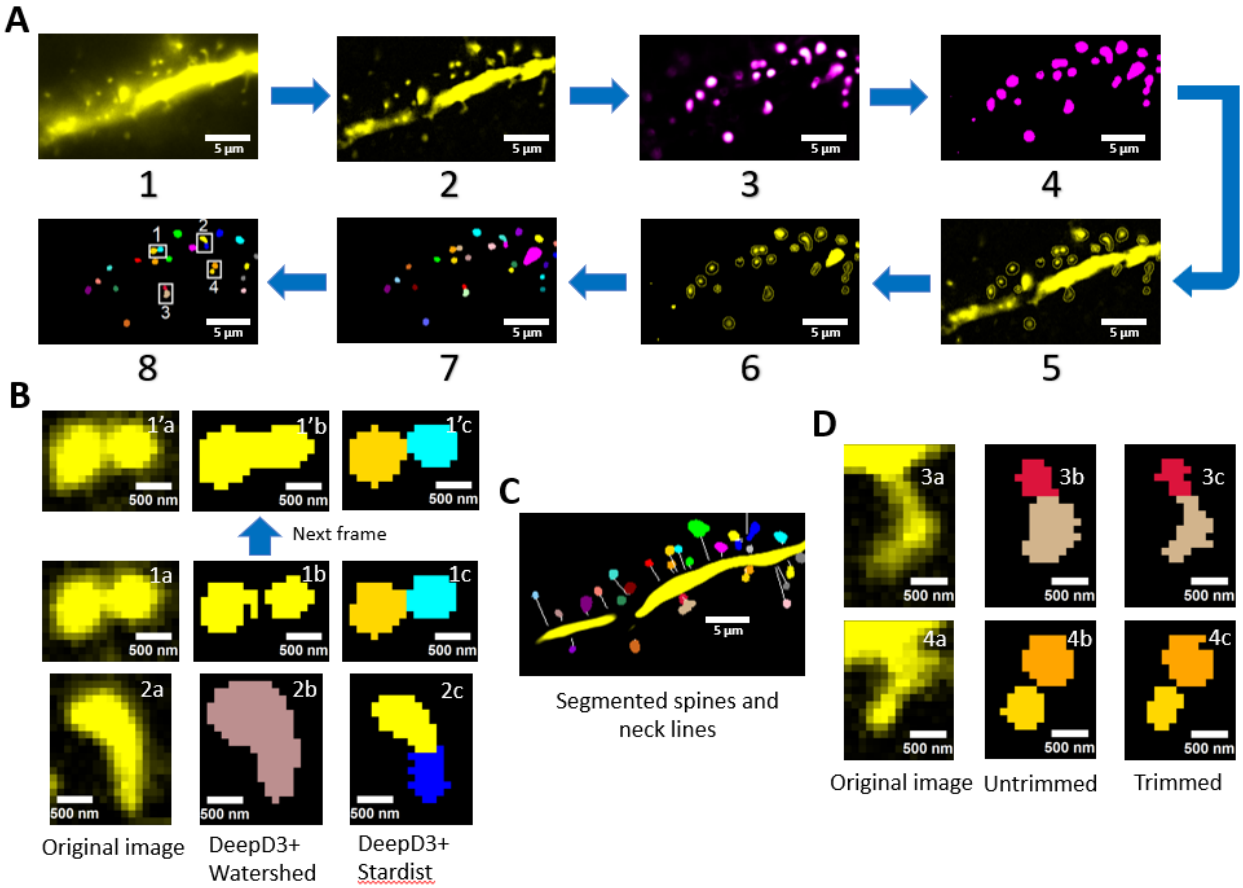

Figure 1. Details of the automatic 3D dendritic spine segmentation approach

(A) The diagram of the workflow of the approach: 1, The starting z-stack (25 nm step size over 2 µm, for this example; yellow represents the fluorescence intensity). 2, Subtraction the background. 3, Applying DeepD3 to assign prediction values to the pixels of its likelihood to be part of a spine (magenta to white represents lower to higher likelihood). 4, Creating a binary mask from a low prediction value threshold. 5, Applying the mask back to the original z-stack. 6, Extracting the fluorescent intensity from the masked regions. 7, Applying Stardist to perform 2D segmentation of the spines in each frame (different colors represent differently segmented spines). 8, Connecting the 2D segmentation across each frame to create the 3D segmentation.

(B) Stardist reliably separates overlapping spines (ROI 1) as well as the spine neck from the head regions (ROI 2), whereas conventional segmentation methods such as Watershed fail.

(C) Segmented results after trimming of spines (ROI 3 and 4) match the image more closely.

(D) The final result of segmented spines and constructed neck lines for the 40 frames (1 µm) projection of the z-stack.

Validation with dSTORM images of dendritic spines

We validated our approach with 3D-dSTORM imaging and manual segmentation of the super-resolution reconstruction, which serves as a “ground truth” for spine segmentation. Before dSTORM imaging, we took diffraction-limited z-stacks of the dendritic segments of hippocampal CA1 neurons expressing Thy1-YFP (Yellow fluorescence protein) in 30 µm thick brain slices (Figure 2A-1). The use of Thy1-YFP enables only a small fraction of neurons to be labeled with YFP so that individual neurons can be examined. YFP, being a poor fluorophore for dSTORM, was labeled with a nanobody to YFP (GBP) conjugated with Alexa647 for dSTORM imaging (Figure 2A-2).[35] We then manually segmented the dSTORM reconstruction (Figure 2A-3) and then compared it with different segmentation methods (DeepD3+Watershed etc.) of the diffraction-limited YFP z-stack images (Figure 2A 4-7).

Because the dSTORM imaging of Alexa647 does not contain enough localizations for reliable manual segmentation of each frame, we used either a 40-frame or a 4-frame maximum intensity projection. That is, a 2D image was created with each pixel taking the highest intensity value along the z-axis. The 40-frame projection involves the segmentations across all z-planes (1 µm), whereas the 4-frame projection involves a tenth as much (100 nm). The idea is that the 4-frame projection, *if* enough localizations are detected, will allow a more precise comparison of the 3D shape of spines since a much smaller range in z is projected.

Specifically, we analyzed the difference from the manual segmentation via dSTORM (i.e., the ground truth) with the segmentation using various alternatives: DeepD3+Stardist (Figure 2A-4), the 3D segmentation function provided by DeepD3 (Figure 2A-5), DeepD3+Watershed (Figure 2A-6), and the commonly used commercial software Imaris (Figure 2A-7). We first compared the spine shape segmentation using intersection over union (IoU), which measures the fraction of pixels matched between the ground truth and the segmentation algorithm. We found an IoU of 0.40 (40% match in segmented pixels) for the 40-frame projection of DeepD3+Stardist. With the large difference in SNR and resolution of widefield fluorescence versus dSTORM,[20] this IoU was considered satisfactory. The original DeepD3 method, compared against human annotation on the same two-photon images, found an IoU of around 0.5. In addition, since IoU does not account for the accurate separation of overlapping spines and the necks of spines, we also compared the accuracy in the percent of spines correctly detected for the different segmentation methods. A spine is correctly detected if it is present in both the ground truth and the segmentation from the method. It is incorrectly

detected if present only in the ground truth (missed detection) or only in the segmentation from the methods (false detection).

Compared to other methods, our approach with DeepD3+Stardist shows significant improvement in dendritic spine segmentation and quantification in the widefield diffraction-limited imaging of thick brain slices. When comparing DeepD3+Stardist with DeepD3+Watershed (Figure 2B and 2C), the IoU was found to be slightly higher (0.38 vs 0.33 or 1.2-fold better for 40-frame IoU, 0.27 vs 0.24 or 1.1-fold better for 4-frame IoU). However, there is a greater improvement in percent accuracy in the spines detected due to the role of Stardist in correctly segmenting the spines (65% vs 46%, or 1.4-fold better) (Figure 2D). Thus, DeepD3+Stardist gives a more accurate quantification of spine number than DeepD3+Watershed. DeepD3+Stardist also yielded better results than the segmentation provided by the DeepD3 program, for comparing the 40-frame projection (0.38 vs 0.25, or 1.5-fold better), the 4-frame projection (0.27 vs 0.10, or 2.7-fold better), and the accuracy in spines detected (65% vs 42%, or 1.5-fold better)(Figure 2C). Lastly, DeepD3+Stardist greatly outperformed Imaris on the widefield images, the commonly used commercial software for confocal or two-photon imaging in spine segmentation—for all three metrics (0.38 vs 0.10 or 3.8-fold better for 40-frame IoU, 0.27 vs 0.05 or 5.4-fold better for 4-frame IoU, 65% vs 32% or 2.0-fold better for detection accuracy) (Figure 2A-2C).

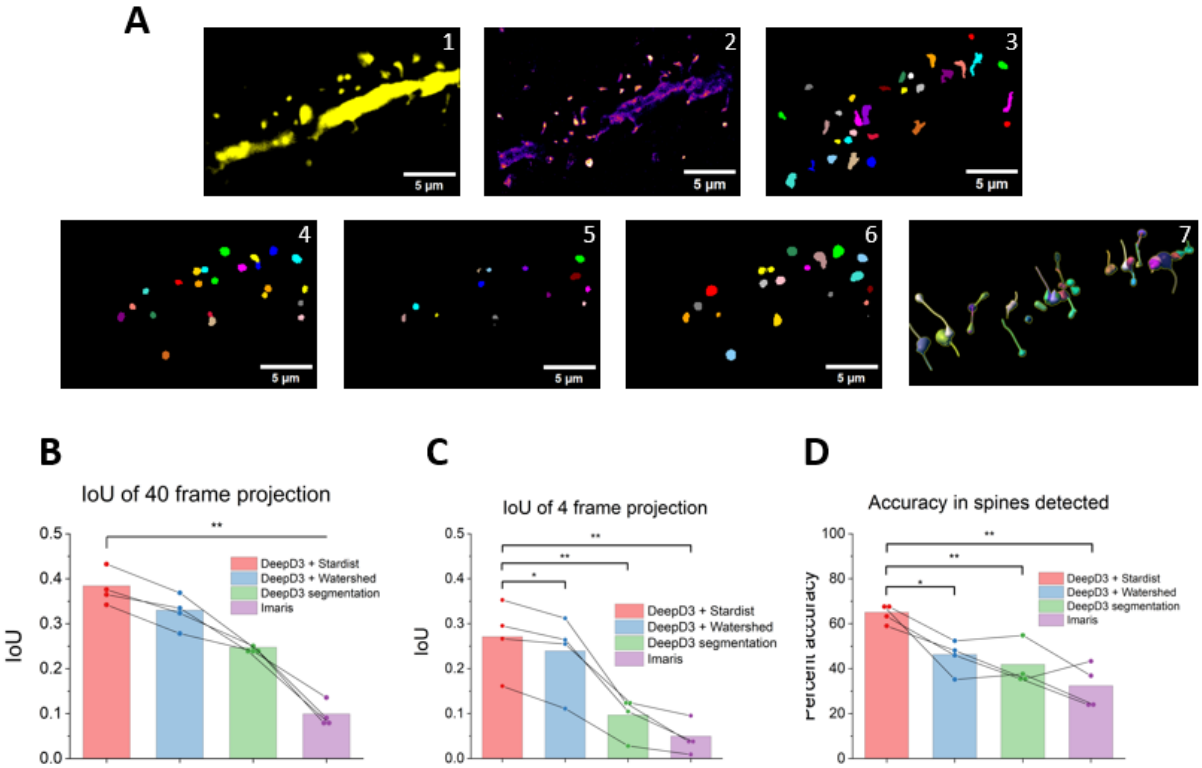

Figure 2. Validation with dSTORM images of dendritic spines

(A) Fluorescent images of dendritic spines and results of different segmentation methods: 1, One frame of the diffraction-limited fluorescent z-stack after background subtraction. 2, STORM reconstruction. 3, Manually segmentation of STORM reconstruction. 4, Segmentation by DeepD3+Stardist. 5, Segmentation by the DeepD3 program. 6, Segmentation by DeepD3+Watershed. 7, Segmentation by Imaris.

(B) Comparison of IoU of 40 frame projection for different methods. The four data points in each method category represent values from four different FOVs. The significance asterisk bracket (**) represents that DeepD3+Stardist is significantly better than every other method. Significance values are obtained from paired sample t tests on values from four different FOVs (alternative hypothesis: mean 1 > mean 2) of DeepD3 + Stardist against other methods.

(C) Comparison of IoU of 4 frame projection for different methods. Significance values are obtained from paired sample t tests on values from four different FOVs (alternative hypothesis: mean 1 > mean 2) of DeepD3 + Stardist against other methods.

(D) Comparison of percent accuracy in the spines correctly detected. Significance values are obtained from paired sample t tests on values from four different FOVs (alternative hypothesis: mean 1 > mean 2) of DeepD3 + Stardist against other methods. Chi-squared tests for contingency table on the total number of spines correctly detected versus incorrectly detected from the four FOVs combined of DeepD3 + Stardist against other methods similarly all give $p < 0.01$ (**).

* : $p < 0.05$, ** : $p < 0.01$. Data is obtained from 4 different FOVs, and a total of 89 spines.

Application to enable spine-specific analysis of dSTORM imaging of synaptic protein PSD-95

We next combined our segmentation approach and dSTORM imaging to analyze the distribution *within* each spine of the post-synaptic density protein PSD-95. We labeled the 30 µm brain slices with a nanobody against PSD-95 conjugated to the dye CF568 and then performed dSTORM imaging on Thy1-YFP neurons in the hippocampus CA1 region. After using DeepD3+Stardist to segment the spines from diffraction-limited YFP fluorescence of the Thy1-YFP neuron, we created automatic analysis to examine and quantify the nanoscale distribution of PSD-95 imaged with dSTORM within spines.

Figure 3A-1 shows an example image of the overlay of the Thy1-YFP neuron and the dSTORM reconstruction of PSD-95, analyzed by the in-situ PSF retrieval (INSPR) program.[36] A zoom-in view of a ROI containing a single spine is also shown in Figure 3A-2. Localizations over the FOV are then assigned to individual spines and dendrites based on the distances to these structures, which is empirically determined as 100 nm for spines and 50 nm for dendrites. Figures 3B-1 show localizations belonging to spines (magenta) and dendrites (cyan) over the entire neuron, with Figure 3B-2 showing for the same spine. Clustering analysis by DBSCAN is performed on the localizations to locate the synaptic nanomodules, followed by secondary DBSCAN clustering analysis on localizations within each nanomodule to identify their composite nanodomains.[37] Figure 3C-1 shows the nanomodules belonging to spines (magnenta) and dendrites (cyan),

with Figure 3C-2 showing that for the same spine. Figure 3C-3 shows the nanodomains (white) within the particular nanomodules in the spine.

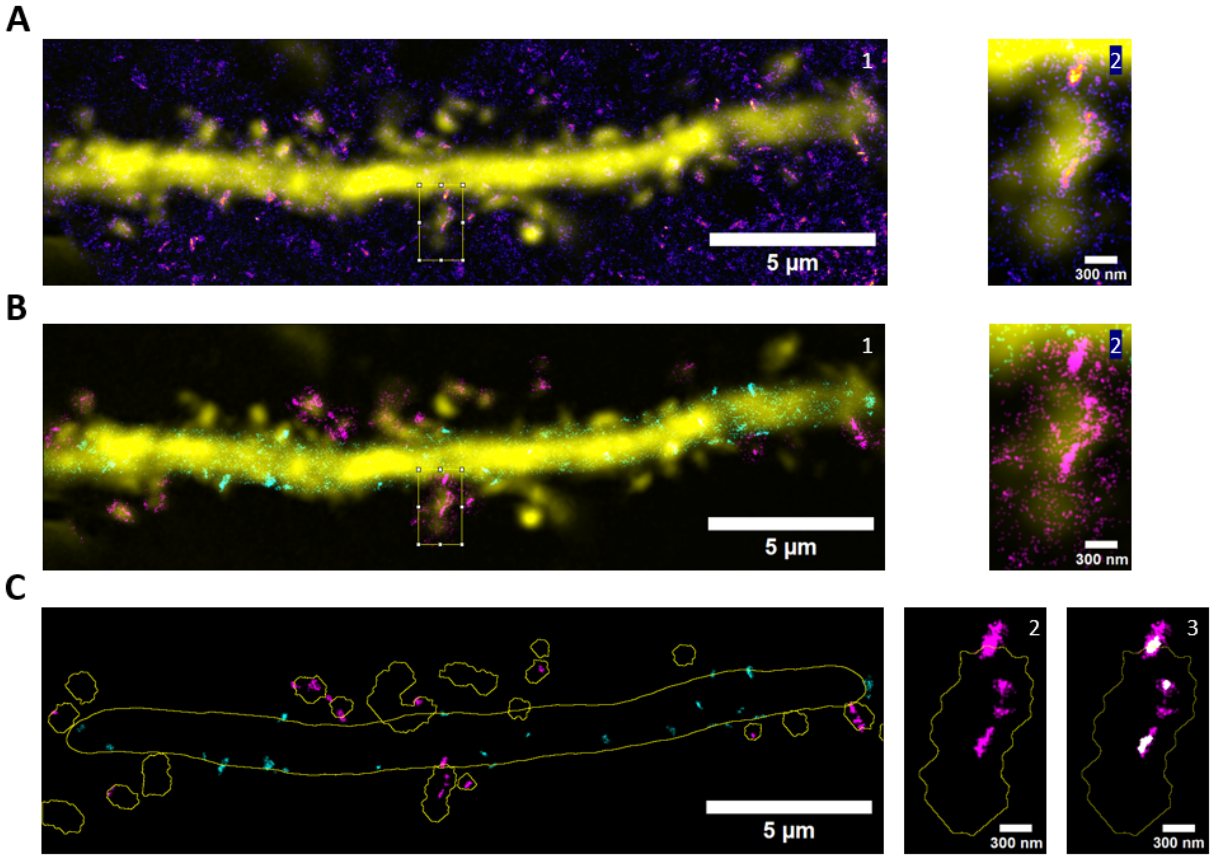

Figure 3. Spine-specific analysis of STORM imaging of synaptic protein PSD-95.

(A) Image of the diffraction-limited YFP fluorescence (yellow) overlaid with the dSTORM reconstruction of PSD-95 (purple to red representing low to high intensity). 1, the whole neuron. 2, ROI containing a single spine.

(B) Image of the diffraction-limited YFP fluorescence (yellow) overlaid with the dSTORM reconstructions of PSD-95 separated as in spines (magenta) and in dendrite (cyan). 1, the whole neuron. 2, ROI containing a single spine.

(C) Image of the nanomodules of PSD-95 separated as in spines (magenta) and in dendrite (cyan). ROI representing contours of spines segmented from the YFP image by DeepD3+Stardist and of dendrite by DeepD3. 1, the whole neuron. 2, ROI containing a single spine. 3, nanodomains (white) within the nanomodules (magenta) in the ROI.

Quantification of PSD-95 nanomodules and nanodomains distribution within spines

The spine segmentation and SMLM analysis allowed us to quantify the distribution of PSD-95 nanomodules within the spines, including how their number correlate with spine size. Surprisingly, two-thirds of the spines contain no nanomodules (Figure 4A). As it is

known that 20% of spines lack PSD-95,[38] some of fraction of the other 80% spines may contain PSD-95 that do not reach the density threshold defined to form nanomodules. Spines containing higher numbers of nanomodules also occur less frequently (Figure 4A). By examining the distribution of spine sizes, we find that slightly over half of the spines without nanomodules have a small volume (defined as < 0.2 μm^3), as compared to one third for spines with nanomodules (Figure 4B). In contrast, spines with nanomodules have twice the fraction of large spines (defined as > 0.6 μm^3) as spines without nanomodules (29% vs 15%) (Figure 4B). Furthermore, the spine size increases with the number of nanomodules contained in the spine (Fig. 4C). This trend is in agreement with the previous STED microscopy study[29] and the understanding that larger spines are generally more mature.[38]

We also determined how the sizes/volumes of nanomodules change with spine sizes. The size of each nanomodule is defined as twice the average distance from each localization in the nanomodule to their center (for example, this size will be 0.75 times the sphere radius for an uniformly distributed sphere). The fraction of nanomodules decreases with increasing sizes, with an average size of 378 nm (Figure 4D). We find no significant dependence for the spine size on the average size of its nanomodules (Figure 4E). As a second measure of nanomodule dimension, nanomodule volume (which gives more 3D information, although the specific value is less intuitive than nanomodule size) is found by the volume of the concave hull, i.e. the boundary, built from localizations inside the nanomodule. The fraction of nanomodules similarly decreases with increasing volumes, with an average volume of 0.023 μm^3 (Figure 4F). In agreement with the trend for nanomodule size, the spine size has no significant dependence on the average volume of its nanomodules (Figure 4G). This indicates that larger spines tend to have more nanomodules instead of having larger individual nanomodules.

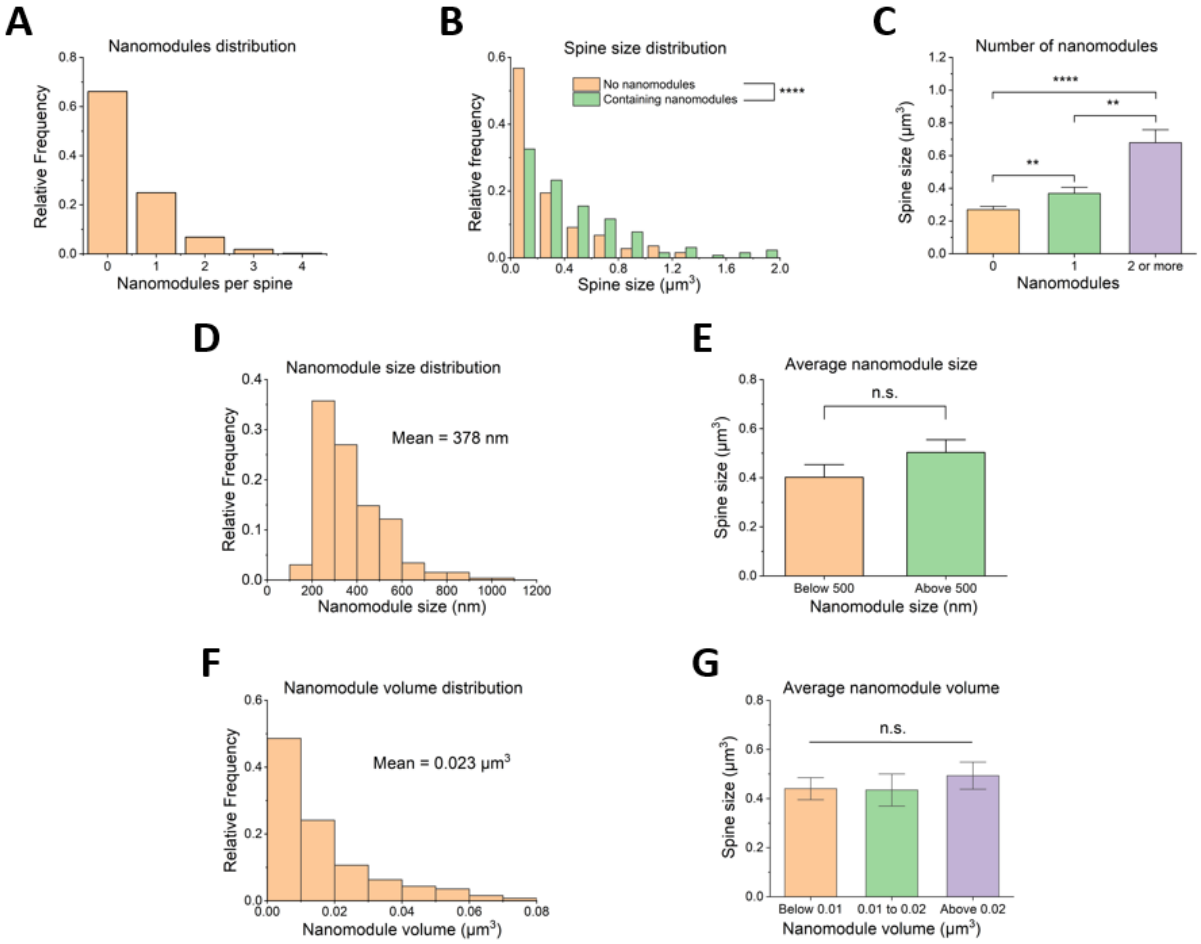

Figure 4. Quantification of nanomodule distribution in spines.

(A) Frequency distribution of the number of nanomodules in spines.

(B) Frequency distribution of spine sizes, separately for spines containing no nanomodules and for spines containing nanomodules.

(C) Spine size versus the number of nanomodules in the spine.

(D) Frequency distribution of nanomodule size.

(E) Spine size versus the average nanomodule size in the spine.

(F) Frequency distribution of nanomodule volume.

(G) Spine size versus the average nanomodule volume in the spine.

Significance values are determined by Kolmogorov–Smirnov tests (mean 1 ≠ mean 2) when comparing two cases (B and E) and Kruskal–Wallis ANOVA when comparing more than two cases (C and G) as the data does not follow a normal distributionns : $p > 0.05$, * : $p < 0.05$, ** : $p < 0.01$, *** : $p < 0.001$, ****: $p < 0.0001$. Data is obtained from 4 independent experiments (from 3 mice), dendritic segments of 12 neurons, and a total of 381 spines. Error bars represent standard error of the mean.

The application of our segmentation approach and dSTORM imaging enabled us to examine the statistics of *nanodomain* distributions inside the *nanomodules* of the spines. Most nanomodules contain one (45%) or two (26%) nanodomains, with a smaller fraction containing zero (9%) or more than two nanodomains (5%) (Figure 5A). Nanomodules containing more nanodomains tend to have larger sizes (Figure 5B) or larger volumes (Figure 5C), except for nanomodules with zero nanodomain. However, for nanomodules with zero nanodomains, it is possible that the PSD-95 is sufficiently spread out to not reach the threshold of a nanodomain.

Additionally, by calculating the ratio of the number of nanodomains to the number of nanomodules in each spine, we find that this ratio does not significantly depend on the spine size (Figure 5D). This is consistent with our other finding that the spine size does not depend on the average size of its nanomodules, because larger nanomodule contains more nanodomains. Therefore, this suggests that the total number of nanodomains, due to increase in the number of nanomodules, alsoincreases with spine size. Indeed, we found that spines containing two to three nanodomains are on average larger than spines containing zero to one nanodomain (Figure 5E) Lastly, using the same calculation done for nanomodules, we found the average size of nanodomains to be 66 nm (Figure 5F) and the average volume to be 8.0×10^{-5} μm^3 (Figure 5G).

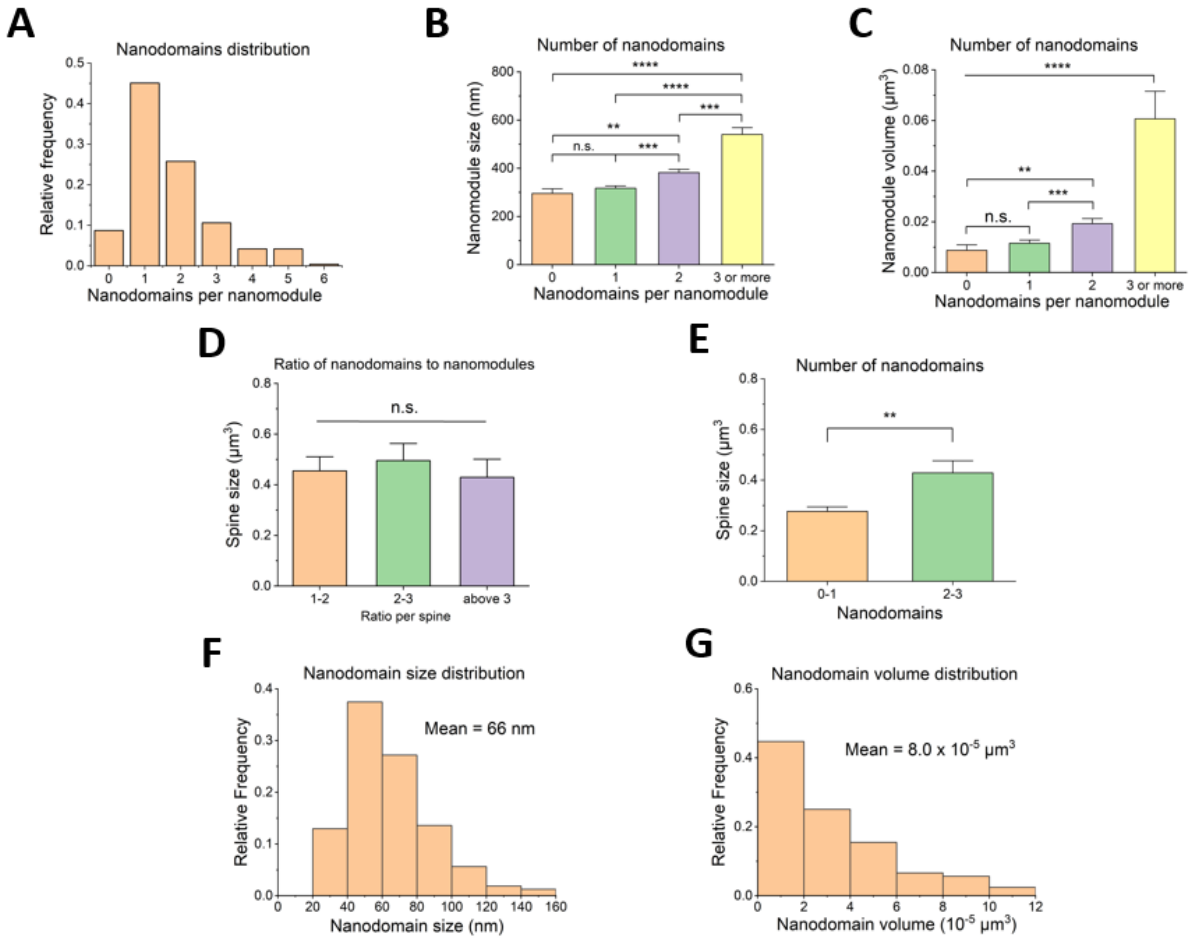

Figure 5. Quantification of nanodomain distribution in spines.

(A) Frequency distribution of the number of nanodomains in spines.

(B) Nanomodule size versus the number of nanodomains in the nanomodule.

(C) Nanomodule volume versus the number of nanodomains in the nanomodule.

(D) Spine size vs ratio of the number of nanodomains to the number of nanomodules in the spine.

(E) Frequency distribution of the nanodomain size.

(F) Frequency distribution of nanodomain volume.

Significance values are determined by Kruskal–Wallis ANOVA. ns : $p > 0.05$, * : $p < 0.05$, ** : $p < 0.01$, *** : $p < 0.001$. Data is obtained from 4 independent experiments (from 3 mice), dendritic segments of 12 neurons, and a total of 381 spines. Error bars represent standard error of the mean.

DISCUSSION

In this work, we established an approach for automatic 3D segmentation of dendritic spines in the widefield diffraction-limited fluorescent images of thick brain slices. Instead

of attempting to obtain the spine structures at the highest resolution as in EM studies,[39] we opted for diffraction-limited widefield images because of the accessibility and relatively fast imaging speed. Unlike current spine segmentation methods which are designed primarily for confocal or two-photon microscopy, DeepD3+Stardist can achieve accurate segmentation results in the low SNR and resolution condition of widefield thick brain slice images. While we have not tested our approach in other imaging conditions, DeepD3+Stardist or the general concept of separately assign prediction and segmentation to two different machine-learning models, may possibly be extended to other difficult conditions to replace the labor-intensive manual segmentation. It should be noted that despite our usage of dSTORM in imaging and segmentating spines for the limited method validation data, applying it for quantitative analysis related to spines would not be desirable. This is because manually segmenting the spines from the dSTORM or other SMLM methods reconstruction from every field-of-view (FOV) imaged would become too labor-intensive. Moreover, in thick brain slices, the number of targets that can imaged together by multicolor dSTORM is limited. More specifically, a good dSTORM dye in the yellow channel for brain slice imaging is lacking, which leaves the channel open for deploying a diffraction-limited dendritic marker (such as Thy1-YFP in our case).

By applying DeepD3+Stardist to diffraction-limited images of neurons and dSTORM of synaptic protein PSD-95 in the same FOV, we quantified the nanoscale distribution of PSD-95 inside spines. In the future, this approach can be applied to quantify the spine-specific distribution of targets beyond the PSD-95 chosen in this study, such as the presynaptic protein RIM1/2 or bassoon to quantifying the number nanocolumns inside spines.[32] One target of particular interest would be AMPA receptors (AMPARs) due to itscrucial role in synaptic plasticity and alteration in multiple neurological diseases.[40,41] Recently, the combination of a novel chemical probe and super-resolution dSTORM has enabled observing the nanoscale distribution of surface-bound AMPARs.[42,43] Our segmentation approach can be applied to study how nanomodules or nanodomains of AMPARs change inside spines. Moreover, examining the correlation of AMPAR with PSD-95 nanostructures inside the dendritic spines in two-color dSTORM imaging will also become possible.

METHOD DETAILS

Animals

All animals were housed, euthanized and dissected in accordance with the guidelines from the Institutional Animal Care and Use Committee (Hee Jung Chung's IACUC protocol #24039) at the University of Illinois at Urbana-Champaign. Thy-YFP-H mice were originally purchased from Jackson Labs (strain #003782).

Acute slice preparation

After sedating the mice with isoflurane and decapitated, the brains were extracted within 5 min of decapitation and mounted onto a Leica vibratome. During sectioning, brains were kept in high osmolarity, ice cold cutting solution (2.5 mM KCl, 2.5 mM $MgCl_2 \cdot 6HO$, 0.5 mM $CaCl_2 \cdot 2H_2O$, 1mM $NaH_2PO_4 \cdot H_2O$, 220 mM sucrose, 25 mM $NaHCO_3$ and 20 mM glucose (dextrose) in ddH2O) with continuous bubbling of 95% O2/5% CO2 gas mixture. 200 µm acute slices of the brain were made using the vibratome and incubated in artificial cerebrospinal fluid (ACSF) (126 mM NaCl, 3 mM KCl, 2 mM $MgSO_4 \cdot 7H_2O$, 2 mM $CaCl_2 \cdot H_2O$, 1mM $NaH_2PO_4 \cdot H_2O$, 25 mM $NaHCO_3$ and 14 mM glucose (dextrose) in ddH_2O) for 30 min at 37^oC under continuous bubbling of 95% O2/5%CO2 gas mixture to stabilize the brain slices. After washing 3x with ACSF, the slices were fixed with 4% PFA in PBS at 4^oC for 24 hours. After fixation, the slices were washed 3x with PBS and stored in PBS for cryosectioning and further labeling.

Nanobody-dye conjugation

FluoTag®-X2 anti-PSD95 nanobody (#N3702-250ug, NanoTag Biotechnologies) was first conjugated to CF®568 maleimide (#92024, Biotium), according to the manufacturer's protocol. The maleimide-conjugated nanobody went through Zeba desalting column (#89882, Thermo Scientific) to get rid of the excess maleimide dye and was subsequently conjugated to CF®568 succinimidyl ester (#92131, Biotium) via NHS reaction to increase the number of dyes per nanobody. The final product was purified using Zeba desalting column (#89882, Thermo Scientific) first, and then with Amicon Ultra Centrifugal Filter (#UFC5005, Millipore Sigma). In the same way, FluoTag®-X2 anti-GFP nanobody (clone 1H1) (#N0302-250ug, NanoTag Biotechnologies) was first conjugated to Alexa Fluor™ 647 C2-maleimide (#A20347, Invitrogen), and then to Alexa Fluor™ 647 NHS Ester (Succinimidyl Ester) (#A20006, Invitrogen), and was purified as before.

Immunohistochemistry

The 200 µm acute brain slices were embedded in optimal cutting temperature (OCT) (#12351753, Fisher Scientific) in cryosectioning molds (#27183, Ted Pella). At this point, slices were either immediately cryo-sectioned or stored at -80^oC for long-term storage. Gelatin-subbed coverslips were prepared for collecting cryosections. Coverslips (#64-0715, Warner Instruments) were first sonicated with 1M KOH for 15 min, followed by sonication for 15 min with 95% ethanol. Coverslips were then dipped in warm ($\sim 50^oC$), filtered 0.5% gelatin and 0.05% chromium potassium sulphate solution in ddH_2O for 1 min and were dried in an oven at 50^oC overnight. 30 µm cryosections of the OCT embedded 200 µm acute slices were made using a Leica cryostat (CM3050 S) and collected on the gelatin-subbed coverslips. Sections at either edge of the 200 µm slice were discarded.

The 30 µm brain slices were incubated in the blocking buffer comprising of 0.2% Triton-X 100 (#648466, Millipore Sigma) and 5% Normal Goat Serum (NGS) (#005-000-121, Jackson Immunoresearch) in PBS or 12 hours at room temperature (RT) on a shaker. The solution was then replaced with either 33 nM anti-PSD95 nanobody conjugated to CF568 dye (#N3705-250ug, NanoTag Biotechnologies) or 18 nM GBP conjugated to Alexa647 dye (#N0302-250ug, NanoTag Biotechnologies) in blocking buffer for 24 hours at RT on a shaker. The slices were then washed 3x with PBS, with 20 min incubation at RT on a shaker between each wash. For slices labeled with anti-PSD95 nanobody, they were postfixed with 4% PFA in PBS for 2 hours at RT on a shaker. PFA was then washed out three times with PBS.

Imaging

For dSTORM imaging, a custom-built inverted microscope was used with astigmatism applied by a deformable mirror for 3D PSD localization. Chromatic aberration shift was calculated using silver-coated coverslip with 100 nm sized holes spaced 1.5 µm away from each other, as well as 100 nm diameter tetraspeck beads (T7279, Thermo Fisher) embedded in 2% agarose gel, to the dSTORM images using custom-written MATLAB code.[44] Coverslips for imaging the samples were mounted onto a holder (A7816, Thermo Fisher) along with the imaging buffer containing 10% Oxyfluor (OF-0005, Oxyrase Inc.) and 10 mM sodium DL-lactate (71720, Sigma-Aldrich) in PBS as the oxygen scavenging system. The imaging buffer also contained 100 mM Cysteamine/Mercaptoethylamine (M9768-5G, Sigma-Aldrich) as a reducing agent and 35% 2-2-thiodiethanol in PBS for refractive index matching. A plastic lid was placed on the holder with mounted coverslips and the imaging chamber was sealed using black aluminum foil tape (T205-1.0, Thorlabs).

Before starting dSTORM imaging, a ±1 µm z-stack with 100 nm step size above and below the plane of focus at the region of interest was collected in the IR (850 nm) transmission imaging CCD camera. This served as the reference stack for real-time drift correction. Then, a z-stack of 96 total frames and step size of 25 nm (total z-length: 96*25 nm ~ 2 µm) was taken of the YFP labeled neuron (FOV size: 25.34 µm x 25.34 µm in 256 x 256 pixels). FOV using 488 nm laser excitation. 50,000 total frames of Alexa fluor 647 dSTORM imaging was collected using 3-4 kW/cm^2 639 nm laser power density, with 20 ms EMCCD exposure time and 100 EM gain. Before imaging CF568, YFP was completely photobleached using 488 nm laser to avoid leakage into the CF568 channel. 75,000 total frames of CF568 dSTORM imaging was collected using 3-4 kW/cm2 561 nm laser power density, with 50 ms EMCCD exposure time and 100 EM gain. For CF568 imaging, the FOV was also illuminated by a 405 nm laser for 50 ms after every four frames, which gradually increased in laser intensity throughout the course of imaging from 10-200 W/cm^2 to maintain the CF568 blinking rate.

Automatic dendritic spine detection and segmentation using DeepD3 + Stardist

The background subtraction function on FIJI (rolling ball radius: 10 pixels, or 10*99 = 990 nm) was applied to the z-stack YFP images to reduce noise. The spine prediction results were obtained using DeepD3 (32 base filter, original resolution model) from the GUI installable from the DeepD3 github: https://github.com/ankilab/DeepD3. The prediction results were exported as tif files. For the DeepD3+Stardist approach introduced, we wrote custom-written python codes that implement the procedures described in the main text. We first applied a threshold to the mask the DeepD3 prediction result for initial pre-Stardist filtering (50 out of 255 max for 8-bit images). After normalizing the masked result to values between 0-100, we then applied Stardist (Stardist model: "2D_versatile_fluo", prob thresh: 0.1, nms thresh: 0.3) as a python library installable from: https://pypi.org/project/stardist/. After the images were segmented independently in each 2D plane, the 2D segmentations were automatically connected in 3D by based on their overlap in consecutive planes. In the case of more than two segmentations overlapping, one segmentation was assigned to the one with the largest overlap in next plane. From the 3D spine segmentations, ones with a low number of total planes were filtered out (min planes: 2). After applying a gaussian blur filter to the dendrite segmentation (sigma: 1), segmented spines which had their centers inside the blurred dendrite segmentation were also filtered, to avoid out-of-focus dendrite parts identified as spines by DeepD3. The segmentation results were stored both as binary and spine-number coded images, as well as 3D ROI file of pixel locations of each spine that could be read and visualized with the 3DSuite pluging in FIJI.[44]

Neck lines were created between segmented spines and the dendrite. When a spine was crossed by the neck line of another spine, it is then assigned as the neck of that spine. For intensity trimming after DeepD3+Stardist, pixels segmented in a spine with a value less than a threshold intensity in the original image were discarded. The threshold intensity was given by a defined ratio times the average intensity of pixels over the segmented spine, and a minimum threshold could also be optionally set to a low value (min intensity ratio: 0.1, min absolute intensity: 50 out of 65535 for 16-bit original images, note the ratio was set low in this case because increasing it did not greatly affect the validation result). This intensity trimming could also be iterated for several rounds (not done in our case).

Dendritic spine segmentation using other approaches

For 3D segmentation using the DeepD3 program itself, the 3D ROI detection function was used on the prediction result (same as default parameters except minimum planes to 2 to match that used in DeepD3+Stardist; ROI building method: floodfill, area threshold: 0.25, peak threshold: 0.80, minimum planes an ROI should span: 2, minimum 3D ROI size [px]: 20, maximum 3D ROI size [px]: 1000, maximum prediction difference

to seed pixel prediction: 0.2, maximum 3D euclidean distance to seed pixel [px]: 2.00). For 3D segmentation using DeepD3+Watershed, we first applied a binary mask with threshold value (150 out of 255 max in 8-bit images, determined empirically) to remove low prediction value pixels from the DeepD3 prediction result. Then, because the Watershed functionality embedded in the DeepD3 program did not work for us, we applied the Watershed function in FIJI to the masked result and connected the 2D segmentations in 3D using the 3DSuite plugin. For 3D segmentation using Imaris 10.1.0, we performed spine segmentation on the background subtracted images. After discarding seed points not around the dendrites or spines on the images or near the edges, we segmented and binarized the spine segmentations (autopath (no loop) no soma with spines, segment seed point (thinnest) diameter: 0.5 µm, segment seed point threshold: 754, spines seed point (thinnest) diameter: 0.4 µm, spine maximum length: 5 µm, spines seed point threshold: 62.8, any unspecified options were as the default).

Validation by dSTORM imaging and manual segmentation

The raw dSTORM images were analyzed by the INSPR program to create single molecule localization data of GBP-Alexa647 (background subtraction (median filter): ON, box size: 32, distance threshold: 13, initial threshold: 10, segmentation threshold: 15, Z-range: -1 to 1 µm with 0.1 µm increment, Z shift mode: OFF, Wyant Zernike order: 64, Bin lowBound: 50, Iteration: 8, Min similarity: 0.6, OTFscale: 2). Reconstructions of dSTORM were created by the ThunderSTORM plugin in FIJI.[45] To account for nanometer chromatic drift or drift ocurred during imaging, dSTORM reconstructions were cross-correlated with the diffraction-limited YFP images and shifted.

For validation, four FOVs containing dendritic segments of THY1-YFP neurons were taken, for a total of 83 dendritic spines as identified in the validation data. We performed manual spines segmentation on the dSTORM reconstructions (10x magnification, or 2560 x 2560 pixels of 9.9 nm pixel size) using FIJI. For comparison against 40-frame maximum projection (20 frames below and above the focal plane, or z-range: 20*25 nm = ±500 nm), a 2D dSTORM reconstruction was used as this range matches the z-range of astigmatism applied. For comparison against 4-frame maximum projection (z-range: 2*25 nm = ±50 nm), 4 frames (with same z-step of 25 nm) also above and below the center of 3D dSTORM reconstruction were combined into one by maximum projection. For manual segmentation, polygon ROIs were first drawn around each spine to set pixels outside to zero. Next, wand (tracing) tool on FIJI was used to trace out the ROI contours of localizations inside the spines, and pixels were binarized as 1 inside the ROIs and 0 outside. For 40-frame projection and in some cases for 4-frame projection, a gaussian blur filter (sigma: 1) to the binarized image, and pixels with non-zero values were set to maximum to binarize the image again. In some cases, a mathematical subtraction to the pixel intensities (5000 out of 65535 for 16-bit images) right before the first binarization was used to remove noisy pixels outside the spine structures.

The projections of segmented diffraction-limited images were scaled up 10x (interpolation: bilinear) to match the dimension of the dSTORM reconstructions (2560 x 2560 pixels). A mathematical subtraction (150 out of 255 max in 8-bit images, determined empirically) was applied to remove low-intensity pixels created from the 10x scaling around edges of objects. Because dSTORM localizations on the edge of FOV could not be detected, spine segmentations near the FOV edges were removed from the calculation of IoU or percent of correctly detected spines. To account for additional drift, the 40-frame maximum projection of the original background subtracted z-stack was cross-correlated with the 2D dSTORM reconstruction. The calculated shift was applied to 40- or 4- frame projections of segmented images using FIJI. To account for axial chromatic drift, we compared the 3D dSTORM reconstruction with the original background subtracted z-stack to establish the corresponding z-frames shift and applied it to the 4-frame projections of segmented images. The IoU was calculated as the fraction of binary pixels (representing it contains part of a spine) in intersection over total pixels in union in the FOV. The number of correctly detected spines was the number of spines present in both images, and that incorrectly detected was the number of spines present only in one image. The percent accuracy in spines correctly detected is given by #correct/(#correct+#incorrect). When spine necks are correctly separated by DeepD3+Stardist, the neck plus and head are counted as one in the calculation.

Spine-specific quantification of synaptic protein distribution imaged by dSTORM

INSPR was used again to obtain the single molecule localization data of anti-PSD95-CF568 from the raw dSTORM images (same parameters as above except distance threshold was 26, instead of 13 due to less dense labeling). Custom-written Python codes were then used to automatically analyze and quantify the single-molecule localization data. DBSCAN algorithm plus an additional minimum requirement on the number of total localizations was used to detect PSD-95 nanomodules (min points: 30, distance: 120 nm, min requirement: 120) in 3D. To account for difference in PSD-95 density in each nanomodule, the density requirement for nanodomains in each nanomodule was determined based on its overall PSD-95 density. By calculating the number of localizations within the 30 nm neighborhood of each localization in the nanomodule, the mean and standard deviation of the number of localizations were found for the nanomodule. DBSCAN was used again to identify nanodomains inside nanomodules (min points: mean+1.5 standard deviation, distance: 30 nm, min requirement: 20).

Concave hulls of nanomodules and nanodomains were built using alphashape (inverse of alpha: 500 nm for nanomodules, 250 nm for nanodomains). The size of one nanomodules or nanodomain was calculated as twice the average distance between each localization to the center of the localizations. The volumes were readily available from the concave hull objects. Nanomodules of PSD-95 were assigned to their nearest

segmented dendrite and spines if a minimum distance requirement was satisfied (50 nm to dendrite and 100 nm to spines). For assigning nanomodules to spines, we only considered spines with their centers in planes (center plane defined as plane that is maximum in the sum of the pixel intensities) within the ± 500 nm focus of imaging, which was roughly the z-range for astigmatism applied. Spine sizes were obtained by the number of voxels segmented as belonging to the spine times the voxel size (99 nm x 99 nm x 25 nm).

ACKNOWLEDGEMENTS

The work is funded by the National Institutes of Health grants RF1AG083625 and R01NS100019 (to P.R.S. and H.J.C.). We thank Yongjae Lee (UIUC) from the Selvin lab for nanobody-dye conjugation. We thank Gregory Tracy (UIUC) and Ki H. Lim (UIUC) from Hee Jung Chung's lab for their help in maintaining the mice.

AUTHOR CONTRIBUTIONS

J.Z., R.V., and P.R.S. designed the experiments. J.Z. wrote the codes for analysis. J.Z. and R.V. performed the experiments and analyzed data. J.Z. and P.R.S. prepared the manuscript. H.J.C. maintained the IACUC protocol and organized the maintenance of the mouse line. All authors participated in manuscript revisioning.

DECLARATION OF INTERESTS

The authors declare no competing interests.

DATA AVAILABILITY

Codes used in analysis and a sample data are attached in the supplementary. All data and any additional information, will be freely available to those who request and provide a feasible data transfer mechanism (such as physical hard disk drives or cloud storage).

REFERENCES

1. Hering, H., and Sheng, M. (2001). Dentritic spines□: structure, dynamics and regulation. Nat Rev Neurosci *2*, 880–888. https://doi.org/10.1038/35104061.

2. Zaccard, C.R., Gippo, I., Song, A., Geula, C., and Penzes, P. (2023). Dendritic spinule-mediated structural synaptic plasticity: Implications for development, aging, and psychiatric disease. Front Mol Neurosci *16*. https://doi.org/10.3389/fnmol.2023.1059730.

3. Holtmaat, A., and Svoboda, K. (2009). Experience-dependent structural synaptic plasticity in the mammalian brain. Nat Rev Neurosci *10*, 647–658. https://doi.org/10.1038/nrn2699.

4. Bhatt, D.H., Zhang, S., and Gan, W.-B. (2009). Dendritic Spine Dynamics. Annu Rev Physiol *71*, 261–282. https://doi.org/10.1146/annurev.physiol.010908.163140.

5. Alimohamadi, H., Bell, M.K., Halpain, S., and Rangamani, P. (2021). Mechanical Principles Governing the Shapes of Dendritic Spines. Front Physiol *12*. https://doi.org/10.3389/fphys.2021.657074.

6. Kasai, H., Ziv, N.E., Okazaki, H., Yagishita, S., and Toyoizumi, T. (2021). Spine dynamics in the brain, mental disorders and artificial neural networks. Nat Rev Neurosci *22*, 407–422. https://doi.org/10.1038/s41583-021-00467-3.

7. Calabrese, B., Wilson, M.S., and Halpain, S. (2006). Development and Regulation of Dendritic Spine Synapses. Physiology *21*, 38–47. https://doi.org/10.1152/physiol.00042.2005.

8. Herms, J., and Dorostkar, M.M. (2016). Dendritic Spine Pathology in Neurodegenerative Diseases. Annual Review of Pathology: Mechanisms of Disease *11*, 221–250. https://doi.org/10.1146/annurev-pathol-012615-044216.

9. Nishiyama, J. (2019). Plasticity of dendritic spines: Molecular function and dysfunction in neurodevelopmental disorders. Psychiatry Clin Neurosci *73*, 541–550. https://doi.org/10.1111/pcn.12899.

10. Forrest, M.P., Parnell, E., and Penzes, P. (2018). Dendritic structural plasticity and neuropsychiatric disease. Nat Rev Neurosci *19*, 215–234. https://doi.org/10.1038/nrn.2018.16.

11. Rodriguez, A., Ehlenberger, D.B., Dickstein, D.L., Hof, P.R., and Wearne, S.L. (2008). Automated three-dimensional detection and shape classification of dendritic spines from fluorescence microscopy images. PLoS One *3*. https://doi.org/10.1371/journal.pone.0001997.

12. Shi, P., Huang, Y., and Hong, J. (2014). Automated three-dimensional reconstruction and morphological analysis of dendritic spines based on semi-supervised learning. Biomed Opt Express *5*, 1541. https://doi.org/10.1364/boe.5.001541.

13. Dickstein, D.L., Dickstein, D.R., Janssen, W.G.M., Hof, P.R., Glaser, J.R., Rodriguez, A., O'Connor, N., Angstman, P., and Tappan, S.J. (2016). Automatic dendritic spine quantification from confocal data with neurolucida 360. Curr Protoc Neurosci *2016*, 1.27.1-1.27.21. https://doi.org/10.1002/cpns.16.

14. Ghani, M.U., Mesadi, F., Kanık, S.D., Argunşah, A.Ö., Hobbiss, A.F., Israely, I., Ünay, D., Taşdizen, T., and Çetin, M. (2017). Dendritic spine classification using shape and appearance features based on two-photon microscopy. J Neurosci Methods *279*, 13–21. https://doi.org/10.1016/j.jneumeth.2016.12.006.

15. Singh, P.K., Hernandez-Herrera, P., Labate, D., and Papadakis, M. (2017). Automated 3-D Detection of Dendritic Spines from In Vivo Two-Photon Image Stacks. Neuroinformatics *15*, 303–319. https://doi.org/10.1007/s12021-017-9332-2.

16. Das, N., Baczynska, E., Bijata, M., Ruszczycki, B., Zeug, A., Plewczynski, D., Saha, P.K., Ponimaskin, E., Wlodarczyk, J., and Basu, S. (2022). 3dSpAn: An interactive software for 3D segmentation and analysis of dendritic spines. Neuroinformatics *20*, 679–698. https://doi.org/10.1007/s12021-021-09549-0.

17. Vidaurre-Gallart, I., Fernaud-Espinosa, I., Cosmin-Toader, N., Talavera-Martínez, L., Martin-Abadal, M., Benavides-Piccione, R., Gonzalez-Cid, Y., Pastor, L., DeFelipe, J., and García-Lorenzo, M. (2022). A Deep Learning-Based Workflow for Dendritic Spine Segmentation. Front Neuroanat *16*. https://doi.org/10.3389/fnana.2022.817903.

18. Argunşah, A.Ö., Erdil, E., Ghani, M.U., Ramiro-Cortés, Y., Hobbiss, A.F., Karayannis, T., Çetin, M., Israely, I., and Ünay, D. (2022). An interactive time series image analysis software for dendritic spines. Sci Rep *12*. https://doi.org/10.1038/s41598-022-16137-y.

19. Ekaterina, P., Peter, V., Smirnova, D., Vyacheslav, C., and Ilya, B. (2023). SpineTool is an open-source software for analysis of morphology of dendritic spines. Sci Rep *13*. https://doi.org/10.1038/s41598-023-37406-4.

20. Fernholz, M.H.P., Guggiana Nilo, D.A., Bonhoeffer, T., and Kist, A.M. (2024). DeepD3, an open framework for automated quantification of dendritic spines. PLoS Comput Biol *20*. https://doi.org/10.1371/journal.pcbi.1011774.

21. Schmidt, U., Weigert, M., Broaddus, C., and Myers, G. (2018). Cell Detection with Star-convex Polygons. https://doi.org/10.1007/978-3-030-00934-2_30.

22. Vincent, L., and Soille, P. (1991). Watersheds in digital spaces: an efficient algorithm based on immersion simulations. IEEE Trans Pattern Anal Mach Intell *13*, 583–598. https://doi.org/10.1109/34.87344.

23. Huang, B., Wang, W., Bates, M., and Zhuang, X. (2008). Three-Dimensional Super-Resolution Imaging by Stochastic Optical Reconstruction Microscopy. Science (1979) *319*, 810–813. https://doi.org/10.1126/science.1153529.

24. Heilemann, M., van de Linde, S., Schüttpelz, M., Kasper, R., Seefeldt, B., Mukherjee, A., Tinnefeld, P., and Sauer, M. (2008). Subdiffraction-Resolution Fluorescence Imaging with Conventional Fluorescent Probes. Angewandte Chemie International Edition *47*, 6172–6176. https://doi.org/10.1002/anie.200802376.

25. Lelek, M., Gyparaki, M.T., Beliu, G., Schueder, F., Griffié, J., Manley, S., Jungmann, R., Sauer, M., Lakadamyali, M., and Zimmer, C. (2021). Single-molecule localization microscopy. Nature Reviews Methods Primers *1*, 39. https://doi.org/10.1038/s43586-021-00038-x.

26. Dani, A., Huang, B., Bergan, J., Dulac, C., and Zhuang, X. (2010). Superresolution Imaging of Chemical Synapses in the Brain. Neuron *68*, 843–856. https://doi.org/10.1016/j.neuron.2010.11.021.

27. Bats, C., Groc, L., and Choquet, D. (2007). The Interaction between Stargazin and PSD-95 Regulates AMPA Receptor Surface Trafficking. Neuron *53*, 719–734. https://doi.org/10.1016/j.neuron.2007.01.030.

28. Lin, Y., Skeberdis, V.A., Francesconi, A., Bennett, M.V.L., and Zukin, R.S. (2004). Postsynaptic Density Protein-95 Regulates NMDA Channel Gating and Surface Expression. The Journal of Neuroscience *24*, 10138–10148. https://doi.org/10.1523/JNEUROSCI.3159-04.2004.

29. Hruska, M., Henderson, N., Le Marchand, S.J., Jafri, H., and Dalva, M.B. (2018). Synaptic nanomodules underlie the organization and plasticity of spine synapses. Nat Neurosci *21*, 671–682. https://doi.org/10.1038/s41593-018-0138-9.

30. MacGillavry, H.D., Song, Y., Raghavachari, S., and Blanpied, T.A. (2013). Nanoscale scaffolding domains within the postsynaptic density concentrate synaptic ampa receptors. Neuron *78*, 615–622. https://doi.org/10.1016/j.neuron.2013.03.009.

31. Nair, D., Hosy, E., Petersen, J.D., Constals, A., Giannone, G., Choquet, D., and Sibarita, J.B. (2013). Super-resolution imaging reveals that AMPA receptors inside synapses are dynamically organized in nanodomains regulated by PSD95. Journal of Neuroscience *33*, 13204–13224. https://doi.org/10.1523/JNEUROSCI.2381-12.2013.

32. Tang, A.-H., Chen, H., Li, T.P., Metzbower, S.R., MacGillavry, H.D., and Blanpied, T.A. (2016). A trans-synaptic nanocolumn aligns neurotransmitter release to receptors. Nature *536*, 210–214. https://doi.org/10.1038/nature19058.

33. Haas, K.T., Compans, B., Letellier, M., Bartol, T.M., Grillo-Bosch, D., Sejnowski, T.J., Sainlos, M., Choquet, D., Thoumine, O., and Hosy, E. (2018). Pre-post

synaptic alignment through neuroligin-1 tunes synaptic transmission efficiency. Elife *7*. https://doi.org/10.7554/eLife.31755.

34. Han, Y., Cao, R., Qin, L., Chen, L.Y., Tang, A.-H., Südhof, T.C., and Zhang, B. (2022). Neuroligin-3 confines AMPA receptors into nanoclusters, thereby controlling synaptic strength at the calyx of Held synapses. Sci Adv *8*. https://doi.org/10.1126/sciadv.abo4173.

35. Rothbauer, U., Zolghadr, K., Tillib, S., Nowak, D., Schermelleh, L., Gahl, A., Backmann, N., Conrath, K., Muyldermans, S., Cardoso, M.C., et al. (2006). Targeting and tracing antigens in live cells with fluorescent nanobodies. Nat Methods *3*, 887–889. https://doi.org/10.1038/nmeth953.

36. Xu, F., Ma, D., MacPherson, K.P., Liu, S., Bu, Y., Wang, Y., Tang, Y., Bi, C., Kwok, T., Chubykin, A.A., et al. (2020). Three-dimensional nanoscopy of whole cells and tissues with in situ point spread function retrieval. Nat Methods *17*, 531–540. https://doi.org/10.1038/s41592-020-0816-x.

37. Ester, M., Kriegel, H.-P., Sander, J., and Xu, X. (1996). A Density-Based Algorithm for Discovering Clusters in Large Spatial Databases with Noise. In KDD'96: Proceedings of the Second International Conference on Knowledge Discovery and Data Mining (AAAI Press), pp. 226–231.

38. Berry, K.P., and Nedivi, E. (2017). Spine Dynamics: Are They All the Same? Neuron *96*, 43–55. https://doi.org/10.1016/j.neuron.2017.08.008.

39. Kuwajima, M., Spacek, J., and Harris, K.M. (2013). Beyond counts and shapes: Studying pathology of dendritic spines in the context of the surrounding neuropil through serial section electron microscopy. Neuroscience *251*, 75–89. https://doi.org/10.1016/j.neuroscience.2012.04.061.

40. Henley, J.M., and Wilkinson, K.A. (2016). Synaptic AMPA receptor composition in development, plasticity and disease. Nat Rev Neurosci *17*, 337–350. https://doi.org/10.1038/nrn.2016.37.

41. Diering, G.H., and Huganir, R.L. (2018). The AMPA Receptor Code of Synaptic Plasticity. Neuron *100*, 314–329. https://doi.org/10.1016/j.neuron.2018.10.018.

42. Wakayama, S., Kiyonaka, S., Arai, I., Kakegawa, W., Matsuda, S., Ibata, K., Nemoto, Y.L., Kusumi, A., Yuzaki, M., and Hamachi, I. (2017). Chemical labelling for visualizing native AMPA receptors in live neurons. Nat Commun *8*, 14850. https://doi.org/10.1038/ncomms14850.

43. Vaidya, R.M., Nall, D.L., Zhang, J., Lee, Y., Ma, D., Huang, F., Kiyonaka, S., Hamachi, I., Chung, H.J., and Selvin, P.R. (2024). Observing nanoscale

organization of native, cell-surface AMPARs in mouse brain slices as a function of brain region and taupathy. Biophys J *123*, 417a. https://doi.org/10.1016/j.bpj.2023.11.2542.

44. Lee, S.H., Jin, C., Cai, E., Ge, P., Ishitsuka, Y., Teng, K.W., de Thomaz, A.A., Nall, D., Baday, M., Jeyifous, O., et al. (2017). Super-resolution imaging of synaptic and Extra-synaptic AMPA receptors with different-sized fluorescent probes. Elife *6*. https://doi.org/10.7554/eLife.27744.

45. Ollion, J., Cochennec, J., Loll, F., Escudé, C., and Boudier, T. (2013). TANGO: a generic tool for high-throughput 3D image analysis for studying nuclear organization. Bioinformatics *29*, 1840–1841. https://doi.org/10.1093/bioinformatics/btt276.

46. Ovesný, M., Křížek, P., Borkovec, J., Švindrych, Z., and Hagen, G.M. (2014). ThunderSTORM: a comprehensive ImageJ plug-in for PALM and STORM data analysis and super-resolution imaging. Bioinformatics *30*, 2389–2390. https://doi.org/10.1093/bioinformatics/btu202.